RSC Advances

PAPER

View Article Online
View Journal | View Issue

Cite this: *RSC Adv.*, 2026, **16**, 7538

Effects of Sn doping content on the structure, morphology, optical and electrical properties of ITO thin films prepared by microwave-assisted spray pyrolysis

Yulun Feng,[bc] Leyuan Zhang,[bc] Haoran Chen,[bc] Lihua Zhang,[*abc] Xin Guo,[bc] Xinya Liu[bc] and Shenghui Guo*[abc]

Received 23rd November 2025
Accepted 27th January 2026

DOI: 10.1039/d5ra09041e

rsc.li/rsc-advances

Indium tin oxide (ITO) thin films with different SnO_2 doping contents (0–20 wt%) were successfully deposited via microwave-assisted spray pyrolysis. The structure, morphology, optical and electrical properties of the as-deposited films were systematically investigated. In contrast to the undoped In_2O_3 film, which exhibits a (222) preferential orientation, the SnO_2-doped ITO films shows a shifted preferential preferential orientation toward (400) along with a reduced (400) diffraction intensity. This orientation change induces significant variations in crystal texture, surface morphology, film thickness, as well as optical and electrical properties. As the SnO_2 doping content increased from 0 to 20 wt%, the thickness of the prepared films decreased continuously, while the surface roughness, the resistance, resistivity, and carrier concentration first decreased significantly and then increased. Notably, the 10 wt% SnO_2-doped ITO film achieved substantially enhanced surface morphology, optical and electrical properties. This film is composed of regular spherical particles with a crystallite size of 43 nm, a root-mean-square roughnessof 5.27 nm, and a total thickness of 310.3 nm. Furthermore, it exhibited an 85.94% transmittance in the visible wavelength range relative to the quartz substrate, a band gap energy of 3.84 eV, a sheet resistance of 7.4 Ω sq^{-1} of, and a resistivity of 1.9×10^{-4} Ω cm, respectively. Compared with ITO films prepared by traditional spray pyrolysis or other method, this film possesses superior electircal conductivity while maintaining comparable optical transmittance. Thus, the ITO film doped with 10 wt% SnO_2 is well-suited for electronic applications, particularly those requiring high-performance transparent conductive electrodes.

1 Introduction

Tin-doped indium oxide, commonly referred to as indium tin oxide (ITO), is a well-known transparent conducting oxide (TCO) material consisting of a composite of indium oxide (In_2O_3) and tin oxide (SnO_2). ITO thin films exhibit excellent optoelectronic performance, featuring high optical transmittance (>80%) in the visible spectral region coupled with ultra-low electrical resistivity (10^{-2} to 10^{-4} Ω cm).[1–3] The high visible-light transmittance of ITO films stems from their wide band gap ($E_g = 3.5$–4.3 eV) at room temperature, whereas their low resistivity is attributed to a high carrier concentration (in the range of 10^{19} to 10^{21} cm^{-3}) induced by oxygen vacancies and Sn dopants.[1,4,5] Owing to this outstanding synergy of optical and electrical properties, ITO films have been widely employed as transparent conductive electrodes in the fabrication of various optoelectronic devices, including liquid crystal displays, flat panel displays, solar cells, sensors, and light-emitting diodes.[6–8]

ITO thin films can be fabricated using various methods, including electron beam evaporation,[6] sputtering,[7,9] sol–gel,[10] atomic layer deposition,[11] and spray pyrolysis.[1,4,12] Among these approaches, the spray pyrolysis (SP) technique is widely adopted owing to its simple fabrication procedure, low production cost, facile control over doping levels, and feasibility for large-area deposition. The SP process involves spraying a precursor solution onto a preheated substrate, where the subsequent chemical reaction proceeds to form metal oxide films on the high-temperature substrate.[13]

The optoelectronic properties of thin films are highly sensitive to deposition-induced microstructure, crystallographic texture, surface morphology and defects, all governed by the deposition method and processing parameters. For SP, rapid and uniform heating of atomized droplets is essential for homogeneous solvent evaporation, precursor thermal decomposition, and subsequent particle growth on the substrate. Microwave heating achieves volumetric heating *via* electromagnetic-to-thermal energy conversion, penetrating droplets to heat them uniformly from inside and out.[14–16,22,23] Conventional heating by conduction and convection, by

[a]*State Key Laboratory of Complex Nonferrous Metal Resources Clean Utilization, Kunming 650093, China*

[b]*Key Laboratory of Unconventional Metallurgy, Ministry of Education, Kunming 650093, China*

[c]*Faculty of Metallurgical and Energy Engineering, Kunming University of Science and Technology, No. 68 Wenchang Road, 121 Street, Kunming, Yunnan 650093, China. E-mail: zhanglihua@kust.edu.cn; 20040051@kust.edu.cn; Tel: +86-0871-65191046*

contrast, causes slow, inefficient energy transfer and large droplet temperature gradients. Microwave-assisted spray pyrolysis (MSP) thus achieves rapid, uniform heating, yielding thin films and particles with enhanced structural and morphological quality. This superior performance has been validated in the synthesis of polycrystalline SnO_2 and SnO_2:F thin films,[14,17] $Ca_3Co_4O_9$ films,[18] Pt/graphene films,[19] CuO/Cu_2O microspheres,[15] hollow Al_2O_3 microspheres,[16] $NiFe_2O_4$ and $ZnAl_2O_4$ nanoparticles,[20] CeO_2 nanoparticles.[21]

Leveraging the advantage of MSP, our previous work,[22,23] confirmed the feasibility of fabricating ITO thin films *via* this technique, which enables the rapid synthesis of ITO films with fundamental structural and optoelectronic properties. However, these preliminary studies focused solely on process feasibility and the effect of microwave heating temperature, without investigating the intrinsic correlation between Sn doping behavior and microwave heating characteristics, nor establishing the structure–performance relationship of MSP-prepared ITO films. As a systematic extension of this prior research, the present work comprehensively studies the effects of Sn doping content on the crystal structure, surface morphology, optical transmittance and electrical conductivity of MSP-fabricated ITO films. We target Sn doping content optimization to improve film quality and enhance the overall optoelectronic performance of ITO films. Specifically aiming to elucidate the regulatory mechanism of Sn doping content on the crystal structure of ITO films under microwave volumetric heating, establish a quantitative structure–optoelectrical performance relationship for MSP-synthesized ITO films, and clarify the mechanism underlying optoelectronic performance degradation at excessive Sn doping levels. Overall, this work advances the further development and practical application of MSP technology in the synthesis of transparent conductive thin films and the fabrication of related optoelectronic materials.

2 Experimental

2.1 Materials

0.05 M precursor solutions were prepared by dissolving indium(III) chloride tetrahydrate ($InCl_3 \cdot 4H_2O$) and tin(IV) chloride pentahydrate ($SnCl_4 \cdot 5H_2O$) in deionized water, yielding [SnO_2]/[SnO_2 + In_2O_3] mass ratios of 0, 5, 10, 15 and 20 wt% in the final ITO films, respectively. A small amount of hydrochloric acid (HCl, 2 mL L^{-1}) was added to enhance the solubility of the precursor mixtures, and each solution was magnetically stirred at 60 °C for 30 min to ensure homogeneous mixing and prevent gelation of the metal salts.

Films were deposited on circular quartz substrates (14 mm diameter and 2 mm thickness). Prior to deposition, all substrates were ultrasonically cleaned in ethanol, acetone and deionized water for 10 min each, then dried with pressurized air.

2.2 Preparation process

Fig. 1 presents the schematic diagram of MSP for ITO thin films deposition on quartz substrates. The prepared precursor solution was loaded into an ultrasonic atomizer (Yunnan Institute of Electronic Industry, China) with a frequency of 1.7 MHz and a spray flow rate of 0.12 L h^{-1}. The solution was ultrasonically atomized into tiny droplets, which were sprayed onto a preheated quartz substrate fixed at the center of a homemade tube-type microwave furnace (described in ref. 22 and 23), with a fixed spraying distance of 30 cm. Compressed air (0.25 m^3 h^{-1}) was used as the carrier gas for droplet delivery and oxidization. The substrate temperature was maintained at 500 ± 2 °C *via* microwave heating (2.45 GHz, 1.5 kW), and the deposition time was fixed at 30 min. Acidic tail gas generated was absorbed by 3 M NaOH before emission.

After deposition, the as-prepared films were naturally cooled to room temperature, collected and sent for characterization and testing. Two replicate experiments were performed under the same deposition parameters, and the relative standard deviation (RSD) is provided in the SI.

2.3 Characterization

The crystal structure was characterized by a Rigaku X-ray diffraction meter (XRD, D/Max 2200) with CuKα radiation (λ = 1.5418 Å). Surface morphology was observed by an Agilent atomic force microscopy (AFM, 5500 AFM/SPM), and film thickness was obtained from cross-sectional images using a Philips scanning electron microscope (SEM, XL-30E). Optical transmittance (300–900 nm) was measured with a Hitachi UV-

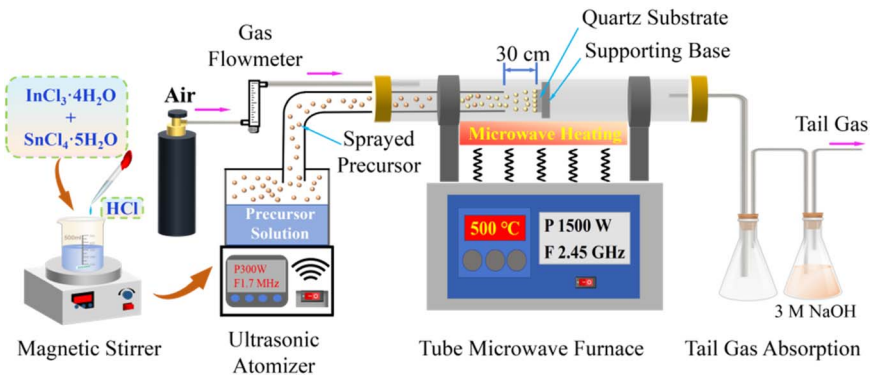

Fig. 1 Schematic diagram of microwave-assisted spray pyrolysis for preparing ITO thin films.

vis spectrophotometer (U-4100). Sheet resistance was tested using a ROOKO four-point probe (FT-341), and carrier concentration was determined *via* the van der Pauw method on a Semishare X3 Hall Effect Measurement System (TEKTRONIX, China).

3 Results and discussion

3.1 Structure

XRD patterns of the deposited thin films with different SnO_2 doping contents (0–20 wt%) are shown in Fig. 2. All films exhibit a cubic In_2O_3 crystal structure (JCPDS PDF #71-2194), with no diffraction peaks corresponding to tin compounds. This indicates that all Sn^{4+} ions incorporate into the In_2O_3 lattice by substituting In^{3+} ions, forming a single-phase solid solution of ITO. Two intensive diffraction peaks at $2\theta = 30.6°$ and 35.5° correspond to the (222) and (400) crystal planes of In_2O_3, respectively, but their intensities differ significantly. The intensity ratio $I_{(400)}/I_{(222)}$ was used to evaluate the effect of SnO_2 content on film texture (Fig. 3). The undoped In_2O_3 film is polycrystalline with a preferred (222) orientation, consistent with standard In_2O_3 powder. In contrast, SnO_2-doped films show a preferred (400) orientation, in agreement with previous reports on traditional spray pyrolysis.[1,2,4] With increasing SnO_2 content (5–20 wt%), the (400) peak intensity gradually decreases while the (222) intensity increases, reducing the $I_{(400)}/I_{(222)}$ ratio from 7.9 to 1.4.

The above variations in diffraction peak intensity and preferred orientation can be well explained by the regulatory effect of SnO_2 doping on oxygen vacancies and lattice structure, which determines the preferred orientation of ITO films together with atomic mobility and high-energy atomic species.[3,24–26] In SnO_2-doped In_2O_3 films, Sn^{4+} ions substitute In^{3+} lattice sites and act as electron donors, inducing a higher density of oxygen vacancies.[29] These vacancies provide

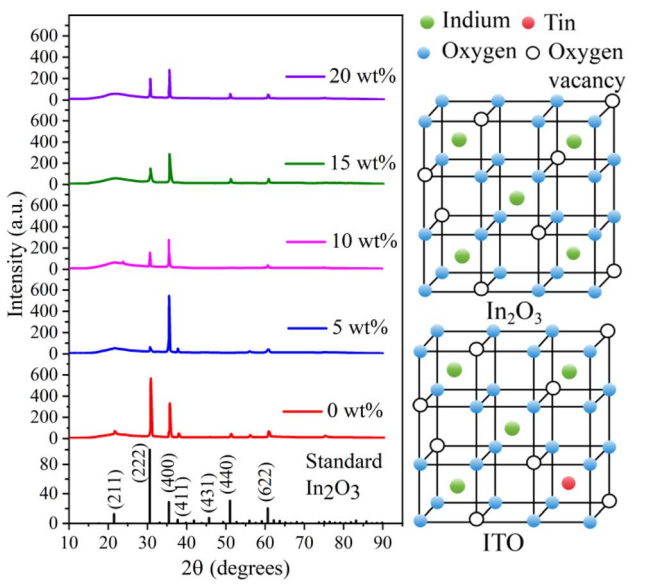

Fig. 2 XRD patterns and crystal structure of the deposited films with SnO_2 doping contents.

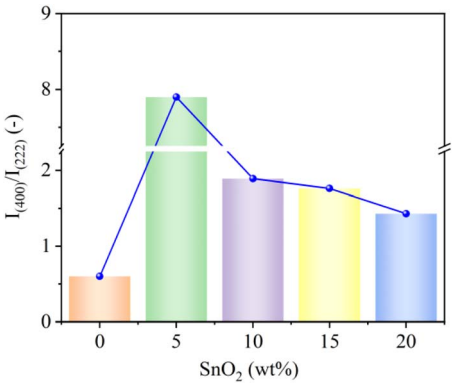

Fig. 3 The intensity ratio $I_{(400)}/I_{(222)}$ for prepared ITO films with SnO_2 doping content.

additional active sites for ionic migration, enhancing film crystallinity and ionic mobility. Since oxygen vacancies preferentially from along the (400) crystal direction in SnO_2-doped films, while (222) orientation prevails in pure In_2O_3 films without such vacancy-induced growth promotion.[3,24] However, excessive SnO_2 doping releases more free electrons, inducing lattice disorders in the In_2O_3 structure.[25,26] This disrupts the preferential growth of (400) orientation and causes competitive and random growth of (400) and (222) orientations, thereby resulting in the decreased diffraction intensity of the dominant (400) peak with further increasing SnO_2 content.

To further evaluate the preferred orientation, grain size and lattice strain, additional calculations were conducted based on the XRD data, as detailed below.[8,12]

$$TC_{(hkl)} = \frac{I_{(hkl)}/I_{0(hkl)}}{(1/N)\sum_{N} I_{(hkl)}/I_{0(hkl)}} \quad (1)$$

$$D = \frac{K\lambda}{\beta \cos\theta} \quad (2)$$

$$\sigma = \frac{\beta \cos\theta}{4K} \quad (3)$$

where $TC_{(hkl)}$, D, and σ denote the texture coefficient of the (hkl) plane, average grain size, and lattice strain, respectively. I, I_0 and N represent the measured diffraction intensity, standard reference intensity, and number of reflections, respectively. In addition, λ, θ, and β correspond to the X-ray wavelength (1.5405 Å for Cu Kα radiation), diffraction angle, and full-width at half-maximum (FWHM) of the diffraction peak, respectively.

Table 1 presents the FWHM, $TC_{(hkl)}$, D, and σ values of the prepared ITO films with different SnO_2 doping contents. FWHM decreases with increasing SnO_2 content, indicating improved ITO film crystallinity during MSP process, which originates from the synergistic effect of Sn^{4+} substitutional doping and microwave volumetric heating. Increased SnO_2 content elevates oxygen vacancies, relieving lattice stress and enhancing microwave absorption efficiency.[35] Microwave heating reduces migration activation energy and facilitates atomic movement, promoting ordered grain growth,[36,37] and reducing defects and

Table 1 Different parameters estimated from XRD studies for prepared films

SnO_2 (wt%)	Preferred orientation	2θ (°)	FWHM (°)	Grain size D (nm)	$TC_{(hkl)}$	Microstrain σ ($\times 10^{-3}$)
Standard In_2O_3	(222)	30.58	—	—	—	—
0	(222)	30.85	0.266	44	0.84	1.12
5	(400)	35.50	0.239	35	2.56	0.99
10	(400)	35.52	0.218	43	2.53	0.95
15	(400)	35.60	0.206	45	2.37	0.86
20	(400)	35.60	0.205	46	2.36	0.85

microstrain (σ),[8] consequently narrowing FWHM, increasing crystallite size (D), and enhancing overall crystallinity.

3.2 Morphology

The surface morphology and root-mean-square (RMS) roughness of the films were analyzed by AFM, as shown in Fig. 4. For undoped In_2O_3 film, unevenly distributed triangular vertebral and spherical grains cover the substrate compactly. Grain growth occurs along preferred nucleation centers, leading to mixed small and large grains, consistent with the high $I_{(400)}/I_{(222)}$ ratio and microstrain in Table 1. This size heterogeneity results in a relatively rough surface with an RMS value of 22.9 nm. For SnO_2-doped ITO films, increasing SnO_2 leads to more regular spherical grains and a flatter surface, with the lowest RMS value (5.27 nm) achieved at 10 wt% SnO_2. However, further increasing SnO_2 to 20 wt% increases the RMS to

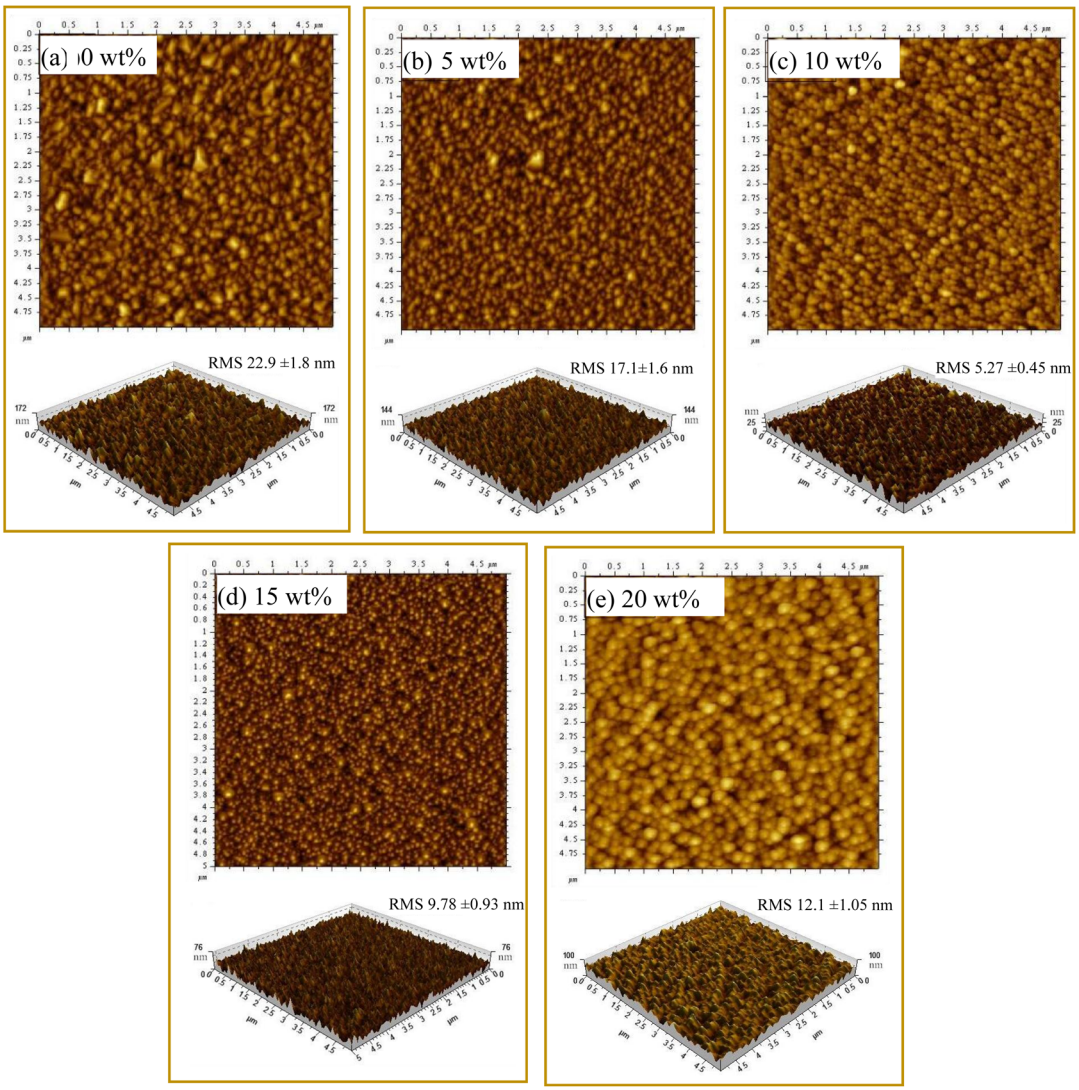

Fig. 4 AFM of the prepared ITO films with SnO_2 doping contents, (a) 0 wt% SnO_2, (b) 5 wt% SnO_2, (c) 10 wt% SnO_2, (d) 15 wt% SnO_2, and (e) 20 wt% SnO_2.

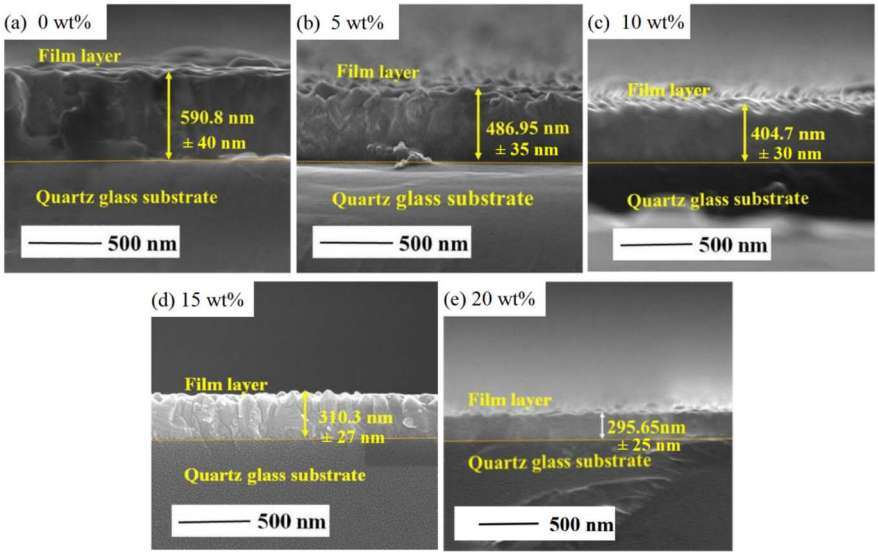

Fig. 5 SEM cross-section images of the prepared films with SnO_2 doping contents, (a) 0 wt% SnO_2, (b) 5 wt% SnO_2, (c) 10 wt% SnO_2, (d) 15 wt% SnO_2, and (e) 20 wt% SnO_2.

12.1 nm. As shown in Table 1, SnO_2 doping improves film crystallinity and increases grain size. The improved crystallinity favors ordered film growth, while larger grains tend to roughen the surface.[2,8] Thus, the optimal 10 wt% SnO_2 doping yields film with the smoothest surfaces and lowest RMS.

Cross-sectional SEM micrographs and film thickness are shown in Fig. 5. Almost all films consist of densely packed columnar grains oriented perpendicularly to the substrate, with thickness decreasing significantly from 590.8 nm to 295.7 nm as SnO_2 content increases from 0 to 20 wt%. This is attributed to improved crystallinity (Fig. 2 and Table 1) and reduced (400) preferred orientation intensity (Fig. 3) with increasing SnO_2 doping. Due to the difference in ionic radii, Sn^{4+} ions (0.69 Å) effectively substitute In^{3+} ions (0.80 Å), filling intrinsic lacunas induced by volatilization of disordered regions in the In_2O_3 matrix.[1] Enhanced crystallinity promotes ordered and well-oriented grains, forming a denser microstructure. Additionally, (400)-oriented grains exhibit higher momentum transfer efficiency and faster growth rates than (222)-oriented grains due to surface energy differences.[9,34] As shown in Fig. 3, the decreasing $I_{(400)}/I_{(222)}$ ratio with increasing SnO_2 content slows overall film growth. Thus, under identical deposition conditions, denser microstructure and slower growth rate lead to gradual thickness reduction with increasing SnO_2 doping.

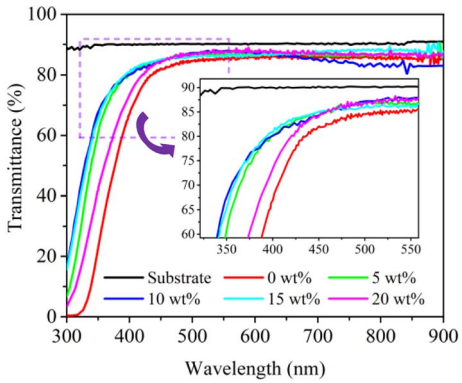

Fig. 6 Transmission spectra for the prepared films with SnO_2 doping contents.

3.3 Optical properties

Fig. 6 shows the transmittance spectra of films with different SnO_2 content, along with the bare quartz substrate spectrum. Key optical parameters, average transmittance in the visible region (T_{av}), T_{av} ratio of film to substrate ($T_{av\text{-}film}/T_{av\text{-}substrate}$), maximum visible transmittance (T_{max}) and transmittance at 550 nm ($T_{550\ nm}$), were derived from these spectra and are listed in Table 2.

As shown in Fig. 6 and Table 2, all films exhibit high transmittance in the visible range (380–780 nm), while transmittance degrades rapidly below 380 nm due to band-to-band transition absorption.[7] The absorption edge shift to shorter wavelength (Burstein–Moss shift), indicating a widened energy band gap (E_g) with increasing SnO_2 dopant.[1] T_{av} increases with SnO_2 content up to 15 wt% and then decreases at 20 wt%. Notably, SnO_2-doped ITO films show T_{av} > 85% relative to the quartz substrate. Normalizing the substrate transmittance to 100% yields T_{av} up to >95%, demonstrating high visible transparency critical for optical applications.

The energy band gap (E_g) of the films was estimated using the Tauc's relation.[7]

$$\alpha h\nu = A(h\nu - E_g)^n \quad (4)$$

where α is the absorption coefficient, $h\nu$ is the photon energy, A is a constant, and $n = 1/2$ for direct band gaps. The absorption coefficient (α) was calculated as described previously.[27]

$$\alpha = \frac{1}{d_T} \ln\left(\frac{1}{T}\right) \quad (5)$$

Table 2 Optical property parameters of the prepared films

Samples with different SnO_2 content (%)	T_{av} (%)	$T_{av\text{-}film}/T_{av\text{-}substrate}$ (%)	T_{max} (%) in the visible zone	Visible wavelength for T_{max} (nm)	$T_{550\ nm}$
Quartz substrate	90.13	100	90.41	706	90.20
0	83.56	92.71	86.59	664	84.82
5	85.83	95.23	88.41	624	86.45
10	85.94	95.35	88.02	537	87.75
15	86.12	95.55	88.41	771	85.85
20	84.68	93.95	89.00	589	87.18

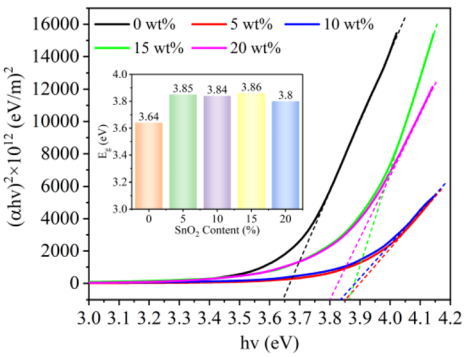

Fig. 7 Variation of $(\alpha h\nu)^2$ *versus* $h\nu$ for the prepared ITO films with SnO_2 doping contents and the inset shows the E_g values.

where d_T is the film thickness and T is the transmittance.

Fig. 7 presents plots of $(\alpha h\nu)^2$ *vs.* $h\nu$ for the prepared films. E_g values were obtained by extrapolating the linear regions of the $(\alpha h\nu)^2$ *vs.* $h\nu$ plots to the $h\nu$ axis (inset of Fig. 7). The undoped In_2O_3 film has an E_g of 3.64 eV, while the 5 wt% SnO_2-doped ITO film shows a marked increase to 3.85 eV. This is consistent with previous reports that undoped (222)-oriented In_2O_3 films prepared by traditional spray pyrolysis have E_g values of 3.53–3.68 eV.[13] With further increasing SnO_2 content, E_g decreases slightly, reaching 3.80 eV at 20 wt% SnO_2.

The band gap shift stems from two competing mechanisms: widening induced by the Burstein–Moss effect and narrowing caused by electron scattering.[1,28] Fig. 8 illustrates the mechanism by which varying SnO_2 contents affect the E_g of the ITO films. Compared to the undoped In_2O_3 film, the E_g of SnO_2-doped In_2O_3 films increases markedly with increasing carrier concentration (Fig. 9c). This phenomenon can be attributed to the Burstein–Moss shift, which occurs when electrons fill higher energy states near the bottom of the conduction band.[9] In contrast, electron scattering is influenced by film crystallinity. As shown in Fig. 2, the improved crystallinity with increasing SnO_2 content corresponds to larger grain sizes and fewer grain boundaries, which reduces the excitation energy for intergranular electron migration, and thus induces E_g narrowing.[29] Consequently, the E_g of the films increases significantly initially and then fluctuates gradually with further increasing SnO_2 doping content, with higher carrier concentrations yielding larger E_g values.

3.4 Electrical properties

The electrical conductivity of the films was characterized in terms of sheet resistance R_s and resistivity ρ, with their correlation expressed by the following equation:

$$\rho = R_s d_T \tag{6}$$

where d_T is the film thickness.

Fig. 9a and b show the variations in R_s and ρ of the films with different SnO_2 doping content. Evidently, SnO_2-doped ITO films exhibits a remarkable conductivity enhancement relative to the

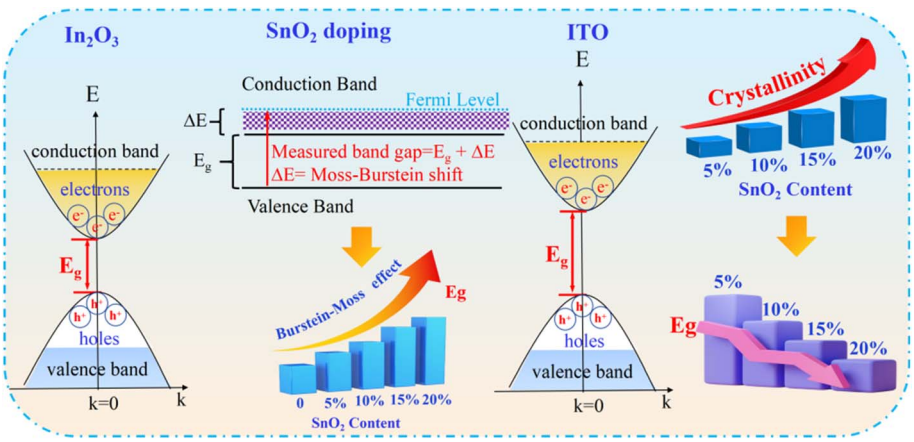

Fig. 8 The mechanism of the effects of varying content of SnO_2 on the optical property of ITO films.

undoped In_2O_3 film. R_s plummeted from 288.8 Ω sq^{-1} for the undoped sample to 7.4 Ω sq^{-1} for the 10 wt% SnO_2-doped film (a ~39-fold reduction), while further increasing SnO_2 to 20 wt% causes a slight rise in R_s to 31.9 Ω sq^{-1}. Correspondingly, ρ decreases sharply and then slightly increases with increasing SnO_2 content, with a minimum value of 1.9×10^{-4} Ω cm achieved for the 10 wt% SnO_2-doped ITO film.

Further analysis indicates that the changes in R_s and ρ are primarily governed by carrier concentration. Fig. 9c presents the carrier concentration (n) and mobility (μ) of the ITO films as a function of SnO_2 content. The n values increase drastically from 6.2×10^{18} cm^{-3} (0 wt% SnO_2) to 1.46×10^{21} cm^{-3} (10 wt% SnO_2), then decline to 4.07×10^{20} cm^{-3} at 20 wt% SnO_2. In contrast, μ shows an opposite trend. The undoped In_2O_3 film exhibits a maximum μ of 59.0 cm^2 V^{-1} s^{-1}, whereas the 5–20 wt% SnO_2-doped ITO films shows slight μ variations in the range of 14.4 to 18.5 cm^2 V^{-1} s^{-1}.

Hall effect measurements confirms the n-type conductivity of the prepared ITO films, with free electrons as the majority charge carriers. The variation in n (*i.e.*, free electrons density) arises from the synergistic effect of SnO_2 doping and oxygen vacancies in the ITO lattice.[5,7] A doubly ionized oxygen vacancy ($O_V^{\cdot\cdot}$) contributes two free electrons ($2e^-$) to the conduction (eqn (7)), while the substitution of In^{3+} by Sn^{4+} in the cubic In_2O_3 lattice (Sn_{In} substitution) donates one free electron (eqn (8)).

$$O_0 \rightarrow O_V^{\cdot\cdot} + 2e^- + \frac{1}{2}O_2(g) \quad (7)$$

$$2SnO_2 \xrightarrow{In_2O_3} 2Sn_{In} + 3O_2 + 2e^- + \frac{1}{2}O_2(g) \quad (8)$$

Compared with the undoped In_2O_3 film, the significantly higher n of SnO_2-doped films stems from the combined effects of oxygen vacancies (eqn (7)) and Sn_{In} substitution (eqn (8)), thus leading to a dramatic reduction in R_s and ρ up to 10 wt% SnO_2 doping. However, further increasing SnO_2 above 10 wt% caused a decline in n, as the reduction in oxygen vacancies induced by increased surface roughness (Fig. 4) outweighs the Sn_{In} substitution from elevated SnO_2 content.[4] A rough surface hinders the effective diffusion of Sn atoms into the In_2O_3 lattice *via* grain boundaries or interstitial sites, which reduces the oxygen vacancies concentration generated by Sn diffusion, subsequently decreasing free electrons and electrical conductivity. For SnO_2-doped ITO films, therefore, a more uniform surface correlates with higher electrical conductivity.

3.5 Comparison of optoelectrical properties

To comprehensively evaluate the suitability of the as-deposited films as transparent conductive oxide (TCO) materials for optoelectronic applications, the figure of merit φ_{TC}, a parameter defined by the combined dependence on optical transmittance and electric resistivity, was calculated using Haacke's equation:[30]

$$\varphi_{TC} = \frac{T^{10}}{R_s} \quad (9)$$

where T denotes optical transmittance and R_s is sheet resistance. Maximizing φ_{TC} is practically significant, as it enables the rational selection of films with high transmittance while retaining low resistance.

Fig. 10 depicts the variation in φ_{TC} of the films with SnO_2 doping content. Incorporation of Sn^{4+} ions into the In_2O_3 lattice leads to a dramatic rise in φ_{TC}, with the maximum φ_{TC} achieved for the 10 wt% SnO_2-doped ITO film, attributable to its low resistance and high transmittance. Further increasing SnO_2 to 20 wt% induces a decline in φ_{TC} due to the elevated resistance. Consequently, 10 wt% SnO_2 is the optimal doping concentration for the ITO films, yielding a favorable balance of high optical transmittance and low electrical resistance.

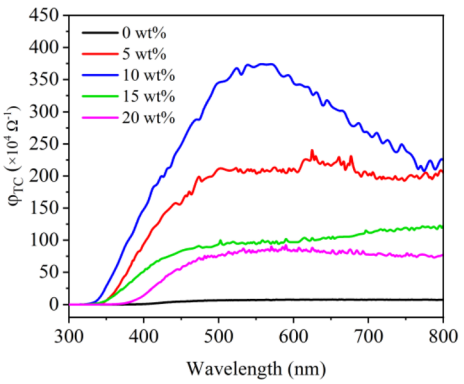

Fig. 10 Figure of merit of the prepared films with SnO_2 doping contents.

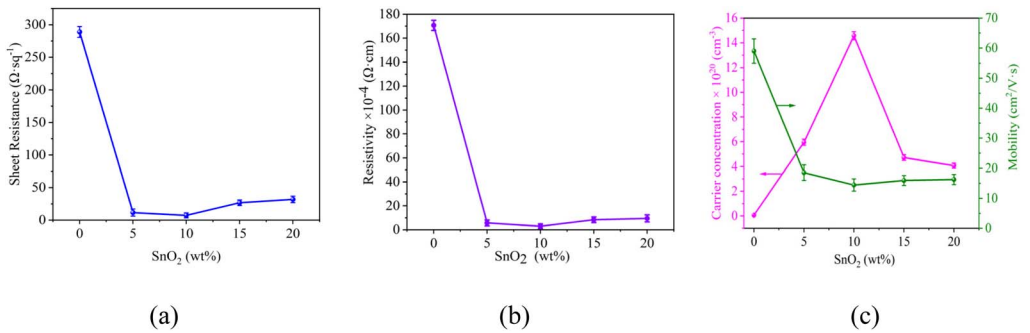

Fig. 9 (a) Sheet resistance, (b) resistivity, and (c) carrier concentration and mobility of the prepared films with SnO_2 doping contents.

Table 3 Optoelectrical properties of ITO films prepared by different methods

Methods	Experimental conditions	Optimized doping content	Film thickness (nm)	E_g (eV)	T_{av} (wavelength range)	R_s (Ω sq^{-1})	ρ ($\times 10^{-4}$ Ω cm)	Ref.
				At optimized conditions				
Microwave-assisted spray pyrolysis	Precursor: 0.05 M ($InCl_3$ + $SnCl_4$), temperature: 773 K, microwave frequency: 2.45 GHz, time: 30 min, substrate: quartz, spraying distance: 30 cm	10 wt% of SnO_2	296–591	3.84	95.35% (380–780 nm)	7.4	1.9	This work
Traditional spray pyrolysis	Precursor solution: $InCl_3$ + $SnCl_2$, temperature: 723–773 K, substrate: glass, spraying distance: 45 cm	5 wt% of Sn	300	—	—	—	3.3	1
Traditional spray pyrolysis	Precursor solution: 6.25–37.5 mM ($InCl_3$ + $SnCl_4$), temperature: 773 K, substrate: glass, spraying distance: 28 cm	5 wt% of Sn	135–205	—	94.4% (380–780 nm)	132	27.1	12
Traditional spray pyrolysis	Precursor solution: $InCl_3$ + $SnCl_4$, temperature: 753 K and 793 K, substrate: Corning 7059 glass	0.023 at% of Sn	—	3.46	80–90% (380–780 nm)	26.6	14.5	4
Traditional d.c. magnetron sputtering	Target: In_2O_3–SnO_2 (90 : 10), temperature: 473 K, sputtering gas: Ar, working pressure: (4–15) $\times 10^{-2}$ torr, time: 20 min, target distance: 52 mm	10 wt% of SnO_2	110	3.87	84.7% (380–780 nm)	—	37	7
Microwave-enhanced d.c. magnetron sputtering	Target: In–Sn (90 : 10), oxygen partial pressure: 3.8–11.7 $\times 10^{-4}$ mbar, substrate: glass, spraying distance: 122 mm	10 wt% Sn	103–106	3.84	85% (1550 nm)	—	22	31
Plasma enhanced atomic layer deposition	Precursor: Cyclopentadienyl indium and tetrakis(dimethylamino)tin with SnO_2-to-In_2O_3 of 0 to 20%, temperature: 523 K, plasma power: 1500 and 3000 W, substrate: Si(100) and glass	1.6 at% of Sn	—	3.8	89% (380–780 nm)	—	2.9	11
Sol–gel	Precursor sol: 0.1 M $In(NO_3)_3$ + 0.01 M SnF_4 with 1 : 1, substrate: glass, spin-coating: 1500 rpm for 30 s, annealing temperature: 473–673 K, annealing time: 2–8 h	In : Sn atomic ratio = 10 : 1	~50	3.85	~80% (380–780 nm)	993	49	10
Microwave sintering	Precursor solution: 0.2 M ($InCl_3$ + $SnCl_2$) with atomic ratios of Sn/(Sn + In) = 0–17.0%, substrate: glass, microwave irradiation: 2.45 GHz, microwave power: 700 W	8.0 at% of Sn	900	—	85% (380–780 nm)	—	5	32

Table 3 (*Contd.*)

Methods	Experimental conditions	Optimized doping content	Film thickness (nm)	E_g (eV)	T_{av} (wavelength range)	R_s (Ω sq^{-1})	ρ ($\times 10^{-4}$ Ω cm)	Ref.
				At optimized conditions				
Electron beam evaporation with post-microwave treatment	Electron beam evaporation: raw materials: ITO tablets with In_2O_3 : SnO_2 of 90 : 10, substrate: Quartz, deposition time: 1000 s, deposition rate: 1 Å s^{-1}, sub-heater temperature: room temperature – 773 K, post-microwave treatment: frequency: 2.4 GHz, power: 600–1000 W, time: 60 s	10 wt% of SnO_2	~100	4.13	98.7% (380–780 nm)	81	—	6
Inkjet-printing	Raw materials: ITO nano-particles, ITO content: 15 wt%, disperse: 72 h ball-mill, high speed mixing at 2000 rpm for 8 min, and ultrasonic homogenizing process for 10 min, substrate: quartz	10 wt% of SnO_2		3.76–3.82	87% (380–780 nm)	517	300	33

The optimized optoelectronic performance of the ITO thin films fabricated *via* this method is compared with that of films prepared by other reported approaches in the literature, as summarized in Table 3. Evidently, the microwave-assisted spray pyrolysis (MSP) method is well-suited for fabricating ITO films with superior optoelectronic performance. Owing to the merits of rapid and homogeneous heating inherent to microwave irradiation, this heating mode has been integrated into magnetron sputtering,[31] sintering,[32] electron beam evaporation[6] and other thin film deposition techniques, which has further improved the optoelectronic properties of the resultant ITO films. This advantageous effect is also validated in the present work. The ITO films doped with 10 wt% SnO_2 prepared by MSP exhibit lower electrical resistance and resistivity and higher optical transmittance relative to those fabricated by alternative methods, including traditional spray pyrolysis,[1,4,12] magnetron sputtering,[7,31] atomic layer deposition,[11] sol–gel,[10] and electron beam evaporation,[6] *etc.*

4 Conclusions

This study investigates the effects of SnO_2 doping content (0–20 wt%) on the structural, morphological, optical and electrical properties of ITO thin films prepared by microwave-assisted spray pyrolysis, with the key conclusions summarized as follows:

(1) XRD analysis confirms all films possess a cubic In_2O_3 crystal structure under microwave volumetric heating. The undoped In_2O_3 film exhibits a (222) preferential orientation, which shifts to (400) upon SnO_2 doping. Increasing SnO_2 content enhances film crystallinity and grain size, while reducing the (400) texture coefficient and microstrain of the films.

(2) AFM and cross-sectional SEM characterizations reveal that the surface homogeneity and flatness first increase then decrease with rising SnO_2 doping content. Film thickness decreases continuously with increasing SnO_2 content, which is attributed to the combined effects of improved crystallinity and a reduced (400) texture coefficient.

(3) Optical measurements show the average optical transmittance (relative to quartz substrate) rises from 83.56% (0 wt% SnO_2) to 86.12% (15 wt% SnO_2), then decreases to 84.68% at 20 wt% SnO_2 doping. The obtained band gap E_g increases remarkably from 3.64 eV (undoped) to 3.85 eV (5 wt% SnO_2), and then fluctuates slightly at ~3.80 eV with further doping up to 20 wt%.

(4) Electrical tests demonstrate that SnO_2 doping significantly enhances the electrical conductivity of ITO films compared to the undoped sample, which originates from the sharp increase in carrier concentration induced by Sn_{In} substitution and oxygen vacancy formation. The sheet resistance R_s and resistivity ρ drop drastically from 288.8 Ω sq^{-1} and 170.7 $\times$ 10^{-4} Ω cm (undoped) to 7.4 Ω sq^{-1} and 1.9 $\times$ 10^{-4} Ω cm at 10 wt% SnO_2 doping, while a slight increase in R_s and ρ is observed with further doping to 20 wt%.

(5) The figure of merit φ_{TC} confirms that SnO_2-doped ITO films have far superior optoelectronic performance to the

undoped In_2O_3 film. 10 wt% SnO_2 is determined as the optimal doping concentration, yielding films with high optical transmittance and low electrical resistance.

Microwave-assisted spray pyrolysis exhibits excellent adaptability for fabricating high-performance ITO films. The 10 wt% SnO_2-doped ITO film shows excellent suitability for diverse optoelectronic applications, particularly those requiring high performance transparent conductive electrodes.

Author contributions

Yulun Feng: writing – review and editing, writing – original draft, formal analysis, data curation; Leyuan Zhang: methodology, formal analysis, writing – review and editing; Haoran Chen: writing – original draft, data curation, formal analysis, resources; Lihua Zhang: visualization, validation, supervision, conceptualization, funding acquisition; Xin Guo: methodology, investigation, formal analysis, conceptualization, resources; Xinya Liu: methodology, investigation, writing – original draft, data curation; Shenghui Guo: project administration, conceptualization, investigation, supervision; Yulun Feng: writing – original draft, resources, data curation, software.

Conflicts of interest

There are no conflicts to declare.

Data availability

Data will be made available upon a reasonable request to the corresponding authors.

Supplementary information (SI): the relative standard deviation (RSD) of surface roughness, thickness and resistivity of the as-prepared ITO films with different SnO_2 doping content. See DOI: https://doi.org/10.1039/d5ra09041e.

Acknowledgements

This work was supported by the Key Technology Research and Development Program of Shandong Province (2023CXGC010903), the National Natural Science Foundation of China (52164040), and the Ten Thousand Talent Plans for Young Top-notch Talents of Yunnan Province (YNWR-QNBJ-2019-150).

References

1 A. E. Hichou, A. Kachouane, J. L. Bubendorff, M. Addou, J. Ebothe, M. Troyon and A. Bougrine, *Thin Solid Films*, 2004, **458**(1–2), 263–268.
2 E. Benamar, M. Rami, C. Messaoudi, D. Sayah and A. Ennaoui, *Sol. Energy Mater. Sol. Cells*, 1999, **56**, 125–139.
3 A. Kosarian, M. Shakiba and E. Farshidi, *IEEJ Trans. Electr. Electron. Eng.*, 2018, **13**, 27–31.
4 K. S. Ramaian, V. S. Raja, A. K. Bhatnagar, R. D. Tomlinson, R. D. Pilkington, A. E. Hill, S. J. Chang, Y. K. Su and F. S. Juang, *Semicond. Sci. Technol.*, 2000, **15**, 676–683.
5 G. Frank and H. Kostlin, *Appl. Phys. A: Solids Surf.*, 1982, **27**, 197–206.
6 T. Kim, M. Chae, D. Lee and H. D. Kim, *Opt. Mater.*, 2024, **149**, 115093.
7 M. J. Zhao, J. F Zhang, Q. H. Huang, W. Y. Wu, M. C. Tseng, S. Y. Lien and W. Z. Zhu, *Vacuum*, 2022, **196**, 110762.
8 C. L. Tien, T. W Lin and S. H. Su, *Opt. Appl.*, 2021, **11**(4), 499–512.
9 C. H. Liang, S. C. Chen, X. D. Qi, C. S. Chen and C. C. Yang, *Thin Solid Films*, 2010, **519**, 345–350.
10 M. Misra, D. K. Hwang, Y. C. Kim, J. M. Myoung and T. I. Lee, *Ceram. Int.*, 2018, **44**, 2927–2933.
11 C. H. Hsu, Z. X. Zhang, C. Y. Shi, P. H. Huang, W. Y. Wu, D. S. Wuu, P. Gao, C. J. Huang, S. Y. Lien and W. Z. Zhu, *J. Mater. Chem. C*, 2022, **10**, 12350–12358.
12 A. V. Moholkar, S. M. Pawar, K. Y. Rajpure, V. Ganesan and C. H. Bhosale, *J. Alloys Compd.*, 2008, **464**, 387–392.
13 A. M. E. Raj, K. C. Lalithambika, V. S. Vidhya, G. Rajagopal, A. Thayumanavan, M. Jayachandran and C. Sanjeeviraja, *Phys. B*, 2008, **403**, 544–554.
14 B. Thomas, K. P. Kumari and S. Deepa, *Sens. Actuators, A*, 2020, **301**, 111755.
15 I. C. Cancellieri, C. P. F. Perdomo, D. N. F. Muche, M. A. L. Cordeiro and R. F. K. Gunnewiek, *Mater. Lett.*, 2023, **350**, 134957.
16 T. Hyodo, M. Murakami, Y. Shimizu and M. Egashira, *J. Eur. Ceram. Soc.*, 2005, **25**, 3563–3572.
17 S. Suchat, J. Prathumsit, A. Sansomboon, G. Gitgeatpong, J. Potisart and P. Prachopchok, *Mater. Today: Proc.*, 2018, **5**, 15160–15165.
18 J. Wangensteen, *Growth and characterization of functional nanoparticulate films by a microwave plasma-assisted spray deposition process*, University of South Florida, Tampa, 2007.
19 E. H. Jo, H. Chang, S. K. Kim, J. H. Choi, S. R. Park, C. M. Lee and H. D. Jang, *Sci. Rep.*, 2016, **6**, 33236.
20 E. K. Nyutu, W. C. Conner, S. M. Auerbach, C. H. Chen and S. L. Suib, *J. Phys. Chem. C*, 2008, **112**, 1407–1414.
21 C. Lv, H. X. Yin, Y. L. Liu, X. X. Chen, M. H. Sun and H. L. Zhao, *Chem. Ind. Chem. Eng. Q.*, 2023, **29**(4), 273–280.
22 L. H. Zhang, J. B. Lan, J. Y. Yang, S. H. Guo, J. H. Peng, L. B. Zhang, S. H. Tian, S. H. Ju and W. B. Xie, *J. Alloys Compd.*, 2017, **728**, 1338–1345.
23 X. W. Bai, H. Yao, C. F. Ren, L. H. Zhang, S. H. Guo and Y. L. Feng, *Mater. Today Commun.*, 2025, **42**, 111516.
24 S. Mala, H. K. E. Latha, H. S. Lalithamba and A. Udayakumar, *Mater. Today*, 2022, **60**, 839–848.
25 N. G. Patel, P. D. Patel and V. S. Vaishnav, *Sens. Actuators, B*, 2003, **9**, 180–189.
26 N. Naghavi, C. Marcel, L. Dupont, C. Guery, C. Maugy and J. M. Tarascon, *Thin Solid Films*, 2002, **419**, 160–165.
27 F. Demichelis, G. Kaniadakis, A. Tagliaferro and E. Tresso, *Appl. Opt.*, 1987, **26**, 1737–1740.
28 I. Hamberg and C. G. Granqvist, *J. Appl. Phys.*, 1986, **60**(11), 123–159.
29 S. Mala, H. K. E. Latha, H. S. Lalithamba and A. Udayakumar, *Mater. Today*, 2022, **60**, 839–848.
30 G. Haacke, *J. Appl. Phys.*, 1976, **47**, 4086–4089.

31 L. J. Meng, E. Crossan, A. Voronov and F. Placido, *Thin Solid Films*, 2002, **422**, 80–86.
32 M. Okuya, N. Ito and K. Shiozaki, *Thin Solid Films*, 2007, **515**, 8656–8659.
33 M. S. Hwang, B. Y. Jeong, J. Moon, S. K. Chun and J. Kim, *Mater. Sci. Eng., B*, 2011, **176**, 1128–1131.
34 J. H. Kim, J. H. Lee, Y. W. Heo, J. J. Kim and J. O. Park, *J. Electroceram.*, 2009, **23**, 169–174.
35 S. H. Kim and W. J. Cho, *J. Nanosci. Nanotechnol.*, 2021, **21**, 1875–1882.
36 P. Yadoji, R. Peelamedu, D. Agrawal and R. Roy, *Mater. Sci. Eng., B*, 2003, **98**, 269–278.
37 J. W. Shin and W. J. Cho, *Phys. Status Solidi A*, 2018, **215**, 1700975.